Int. J. Electrochem. Sci., 13 **(2018)** 7545 – 7557, doi: 10.20964/2018.08.29

International Journal of
ELECTROCHEMICAL
SCIENCE
www.electrochemsci.org

Na^+ and Fe^{3+} Co Doped cathode materials with high electrochemical performances

Min Yuan[1,3], *Hong Ling*[2], *Wei Zeng*[1,3], *Gang Lin*[1,3], *Yanwei Li*[1,3], *Bin Huang*[1,3], *Shunhua Xiao*[1,3,*]

[1] Guangxi Key Laboratory of Electrochemical and Magneto-chemical Functional Materials, College of Chemistry and Bioengineering, Guilin University of Technology, Guilin 541004, China
[2] Department of Mathematics and Information Science, North China University of Water Resources and Electric Power, Zhengzhou 450045, People's Republic of China
[3] Guilin University of Technology, Collaborative Innovation Center for Exploration of Hidden Nonferrous Metal Deposits and Development of New Materials in Guangxi, Guilin University of Technology, Guilin 541004, China
[*]E-mail: 420466855@qq.com

Received: 6 April 2018 / *Accepted:* 10 May 2018 / *Published:* 5 July 2018

In the present work, nanoscale spherical MnO_2 was prepared by hydrothermal method and used as precursor. Then spherical $LiMn_2O_4$, $LiFe_{0.06}Mn_{1.94}O_4$ and $LiNa_{0.06}Mn_{1.94}Fe_{0.06}O_4$ were synthesized by 2-step sintering method. Physical chemical characterization and electrochemical performance tests were carried out with various methods such as X-ray diffraction(XRD), scanning electron microscopy(SEM), Electrochemical Impedance Spectroscopy(EIS), Cyclic Voltammetry(CV) and charge-discharge cycling test. The results indicated that $LiNa_{0.06}Mn_{1.94}Fe_{0.06}O_4$ has better rate cycling performance than $LiMn_2O_4$. Because it has stable crystal structure and the particles are smaller (about 160 nm). After 100 cycles at 0.5 C rate, the discharge capacity of $LiNa_{0.06}Mn_{1.94}Fe_{0.06}O_4$ was 108.0mAh/g, while that of $LiMn_2O_4$ was only 92.2mAh/g. Their retaining capacities were 90.91% and 74.12%, respectively. At 10 C rate, the former has better discharge (34.3mAh/g) than that of the latter. This paper also shows that the composite doping of Na^+ and Fe^{3+} has a positive effect on the Li^+ diffusion coefficient and charge transfer resistance.

Keywords: Hydrothermal; $LiMn_2O_4$; Composite doping; Electrochemical performances

1. INTRODUCTION

Nowadays, as the key power supply for laptops, smart phones and digital cameras, lithium-ion batteries have become one of research hot spots. Compared with lead-acid batteries and Ni-MH batteries, lithium-ion batteries have many advantages such as high working voltage, high energy

/density, long cycle life and no memory effect [1-3]. As the cathode materials in lithium-ion batteries, $LiCoO_2$ has been studied for a long time. However, it has poor safety, high pollution and high price [4-7]. Cathode materials, such as $LiNiO_2$, $LiMn_2O_4$ and $LiFePO_4$, have been studied recently [8-11]. $LiMn_2O_4$, which takes place of $LiCoO_2$ and applied to business, is considered to be the cathode materials due to its low cost, environmental performance and high safety. However, its capacity attenuates seriously during the charge-discharge process [12-16] as a result of the dissolution of Mn in electrolyte, the decomposition of electrolyte and Jahn-Teller effect.

At present, in order to solve the problem about the serious capacity attenuation of $LiMn_2O_4$, researches are focusing on the following aspects: improving synthesis method, doping and coating. Some transition elements or rare earth elements, such as Fe, Al, Mg, Cu, Zn, Ni, Cr and Co [17-22], can be used to cationic doping. The introduction of Na^+ replaces the part of Li^+ in the 8a position of tetrahedron [23]. And then the intercalation/deintercalation of Li^+ during the charge-discharge process prevents the collapse of the structure caused by the lattice shrinkage and expansion. Therefore, it can reduce the dissolution of Mn^{3+} during the charge-discharge process and improve the capacity to some extent. After the introduction of Fe, Fe^{3+} will take the place of some Mn^{3+}, causing the loss of partial capacity. Meanwhile, as the improvement of average valence of Mn, the dissolution of Mn^{3+} and the Jahn-Teller distortion effect can be restrained. Therefore, the crystal structure of materials is more stable and the recycling performance of cathode materials can be improved [24-25].

The nanometer spherical manganese dioxide was synthesized by hydrothermal method. The spiny spherical structure of MnO_2 had bigger surface area, thus enlarged the contact area with Li^+ dopants, and formed spherical products [26-30]. During the charge-discharge process, the intercalation/deintercalation behavior of Li ion could occur on the electrode surface. The bigger surface of the spherical $LiMn_2O_4$ provided a larger area between cathode materials and electrolyte, and shortened the diffusion path of Li^+, thus enhanced the utilization of active substance [31-33]. From the aspect of dynamic, spherical structure helped improve the intercalation/deintercalation behavior of Li^+. Moreover, spherical spinel lithium manganate had higher energy density and power density, thereby gave outstanding electrochemical performances [34-38].

2. EXPERIMENT

2.1. Preparation of materials

$MnSO_4 \cdot H_2O$, $Na_2S_2O_8$ and NH_4Cl were weighed proportionally and dissolved in distilled water. At room temperature, the solution was stirred in a constant temperature magnetic mixer for a period of time till the solution became clear. Then the solution was transferred into a 100 mL PTFE inner tank and the tank was sealed in an autoclave. The autoclave was kept in an oven at 130°C for 15 h and cooled naturally to room temperature. The solution was filtered and washed 3 times with deionized water and ethanol absolute, respectively. After the washing, the black deposit was dried at 90°C for 18 h, and then MnO_2 precursor was gained.

According to the molar ratio of Li_2CO_3, Fe_2O_3, NaOH and MnO_2 precursor, three mixtures were gained. After grinded for a period of time in a agate mortar, ethanol absolute was added during the grinding. Then the three mixtures were put into a Muffle furnace and pre-sintered for 5 h at 500℃. After that, the three mixtures were grinded fully and sintered for 16 h at 750℃, and then cooled to room temperature, the three cathode materials ($LiMn_2O_4$, $LiMn_{1.94}Fe_{0.06}O_4$ and $LiNa_{0.06}Fe_{0.06}Mn_{1.94}O_4$) were gained.

2.2. Structure characterization and electrochemical measurements

The X-ray small-angle diffraction spectra of the samples were obtained using a PANalytical X' Pert^3 Powder diffractometer with a PI Xcel detector. The X-ray generator was operated at 40 kV and 40 mA, using the Cu Kα line at 1.54056 Å as the radiation source. Samples were scanned from 10° to 80° (2θ) and in stage sizes of 0.02626°, with scanning speed of 0.1347°/s. Divergence slit: Fixed slit 1/32°, Incident beam path anti-scatter slit: Fixed slit 1/16°, Diffraction beam path anti-scatter slit: AS slit 7.5mm. S-4800 scanning electron microscope (Japanese Electronics Corp) was used to observe and analyze the morphology of samples.

Active materials, PVDF and acetylene black were weighed at a mass ratio (8: 1: 1) and grinded for a period of time, then N-methyl-2-pyrrolidone was added. Finally, electrode slurry was gained. The slurry was spread on the aluminum foil homogeneously. The foil was dried for 16 h at 110℃ and cut into a wafer electrode (15 mm in diameter). A Li disk worked as negative electrode. Celgard2400 polypropylene microporous membrane was used as the diaphragm, and an electrolyte was composed of 1M $LiPF_6$ in a mixture of dimethyl carbonate (DMC)/ethylene carbonate (EC) (volume ratio of 1:1). They were assembled into button cells (CR2016) in a glove box filled with argon. To test the material's cycling and rate performances, Land CT2001A Battery Testing System was employed to characterize the charge-discharge property in the range of 3.0~4.4 V. Cyclic Voltammetry (CV) and electrochemical impedance spectroscopy (EIS) were carried out in electrochemical workstation (CHI660A), respectively.

3. RESULTS AND DISCUSSION

3.1 Phase composition and morphology

Fig. 1(a) was the XRD pattern of MnO_2 and consistent with JCPDS Card No.24-0735, thus MnO_2 belonged to β type. Fig. 1(b) showed the XRD patterns of $LiMn_2O_4$, $LiMn_{1.94}Fe_{0.06}O_4$ and $LiNa_{0.06}Mn_{1.94}Fe_{0.06}O_4$. The diffraction peaks of $LiMn_{1.94}Fe_{0.06}O_4$ and $LiNa_{0.06}Mn_{1.94}Fe_{0.06}O_4$ were consistent with JCPDS Card No.35-0782 of spinel $LiMn_2O_4$. Therefore, they had cubical spinel structure and belonged to Fd3m cubic system, indicating that Na^+ and Fe^{3+} had inserted into the spinel lattice and the peaks became sharper after the addition of Na^+. It could be seen from Table 1 that the lattice parameter of $LiMn_2O_4$ was a=b=c=8.2426 Å from the calculation, and the unit cell volume was 560.01 Å^3. The lattice parameters of $LMn_{1.94}Fe_{0.06}O_4$ and $LiNa_{0.06}Mn_{1.94}Fe_{0.06}O_4$ were 8.2452 Å, 8.2460Å respectively, and the unit cell volumes of them were 560.53Å^3, 560.70Å^3, respectively. It indicated that the lattice parameter and the unit cell volume were bigger after the addition of Na^+ and Fe^{3+}. Fig.1（c）was the enlarged peak (111) of samples, it could be seen that 2θ (111, $LiMn_2O_4$) ＞2θ

(111, $LiMn_{1.94}Fe_{0.06}O_4$) $> 2\theta$ (111, $LiNa_{0.06}Mn_{1.94}Fe_{0.06}O_4$), which indicated that the 2θ diffraction angles of $LiMn_{1.94}Fe_{0.06}O_4$ and $LiNa_{0.06}Mn_{1.94}Fe_{0.06}O_4$ shifted toward left, it is attributed to the embedding of metal ions and the resulting increase of lattice parameter.

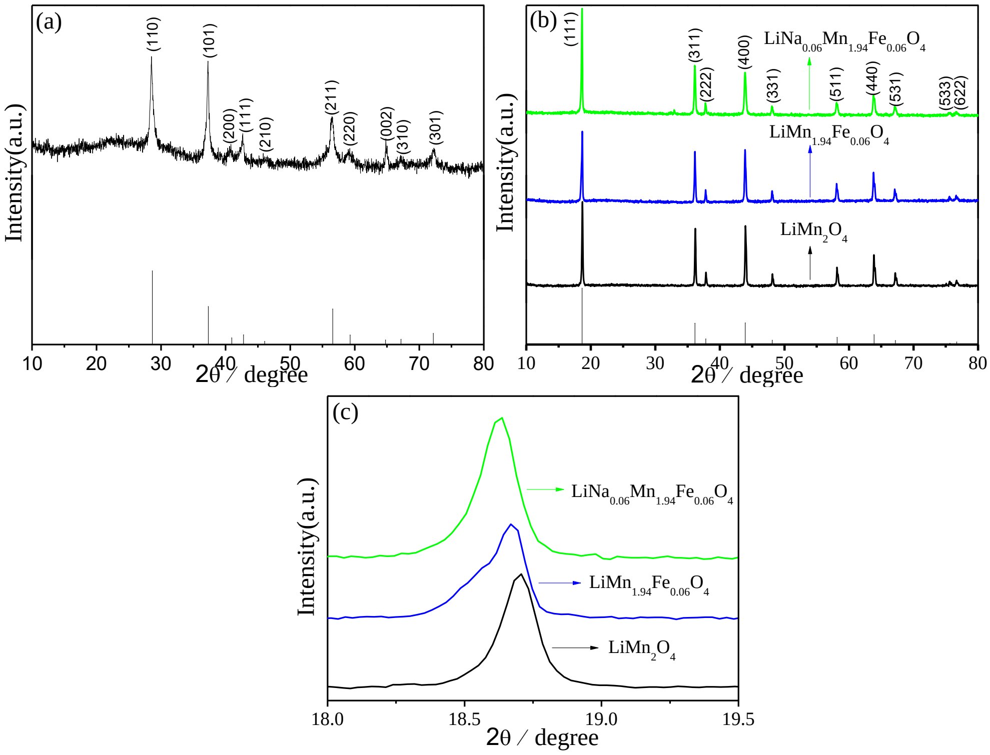

Figure 1. XRD patterns of MnO_2 (a), XRD patterns of $LiMn_2O_4$, $LiMn_{1.94}Fe_{0.06}O_4$ and $LiNa_{0.06}Mn_{1.94}Fe_{0.06}O_4$ (b), enlarged peak (111) of samples (c)

Table 1. Lattice parameters of samples

Samples	Lattice parameter (*Å*)	Unit cell volume (*Å*^{3})
$LiMn_2O_4$	8.2426	560.01
$LiMn_{1.94}Fe_{0.06}O_4$	8.2452	560.53
$LiNa_{0.06}Mn_{1.94}Fe_{0.06}O_4$	8.2460	560.70

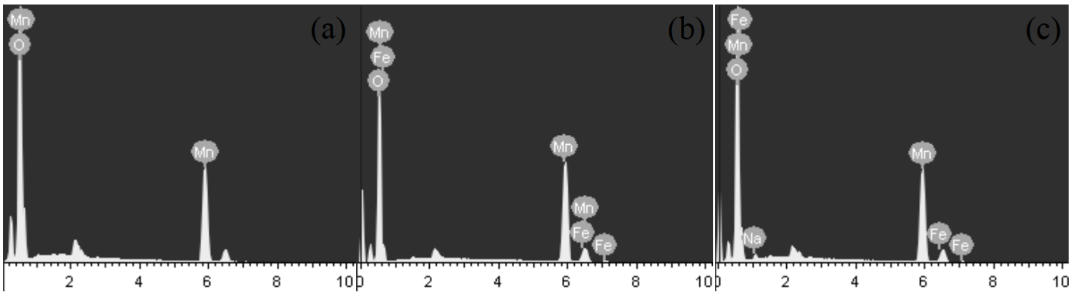

Figure 2. EDS of (a) $LiMn_2O_4$, (b) $LiMn_{1.94}Fe_{0.06}O_4$ and (c) $LiNa_{0.06}Mn_{1.94}Fe_{0.06}O_4$

EDS of (a) $LiMn_2O_4$, (b) $LiMn_{1.94}Fe_{0.06}O_4$ and (c) $LiNa_{0.06}Mn_{1.94}Fe_{0.06}O_4$ were showed in Fig. 2. Compared with the EDS of $LiMn_2O_4$, there were characteristic peaks of Fe in the EDS of $LiMn_{1.94}Fe_{0.06}O_4$ and characteristic peaks of Na and Fe in the EDS of $LiNa_{0.06}Mn_{1.94}Fe_{0.06}O_4$.

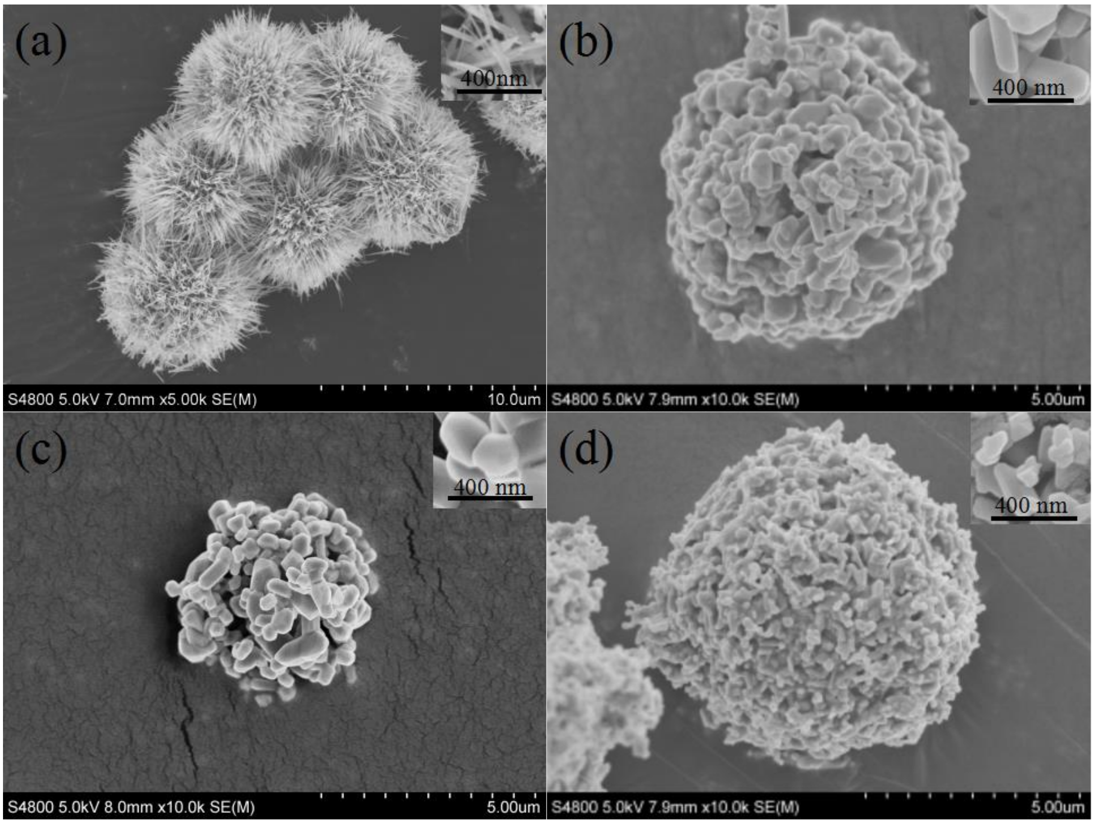

Figure 3. SEM images of (a) MnO_2, (b) $LiMn_2O_4$, (c) $LiMn_{1.94}Fe_{0.06}O_4$, (d) $LiNa_{0.06}Mn_{1.94}Fe_{0.06}O_4$

Fig. 3(a) showed the SEM images of the MnO_2 precursor. As no additive or adjuvant was used in the experiment, the reaction temperature and the rate of reaction were low. The steady reaction environment was beneficial for the agglomeration of crystal nucleus, which continued to form the slender nanometer sticks (shown in the top right illustration). The sticks radiated outwards from the center, thus the whole structure looked like a spiny sphere. The diameter of a nanometer stick was about 40 nm and the diameter of spiny sphere was about 4μm. Fig. 3(b), Fig. 3(c) and Fig.3(d) were the SEM images of $LiMn_2O_4$, $LiMn_{1.94}Fe_{0.06}O_4$ and $LiNa_{0.06}Mn_{1.94}Fe_{0.06}O_4$ samples, respectively. It could be seen that these three samples were reunited by granular structures. The sizes of granular structures of $LiMn_2O_4$ ranged from 180 nm to 400 nm. The granular structures of the $LiMn_{1.94}Fe_{0.06}O_4$ and $LiNa_{0.06}Mn_{1.94}Fe_{0.06}O_4$ samples were regular and uniform. The sizes of granular structures of the $LiMn_{1.94}Fe_{0.06}O_4$ sample were about 300 nm, while the particle sizes of the $LiNa_{0.06}Mn_{1.94}Fe_{0.06}O_4$ samples were the smallest (about 160 nm). These minor sized granular structures could effectively shorten the diffusion route of Li^+ and improve the diffusion rate of Li^+ [39-40].

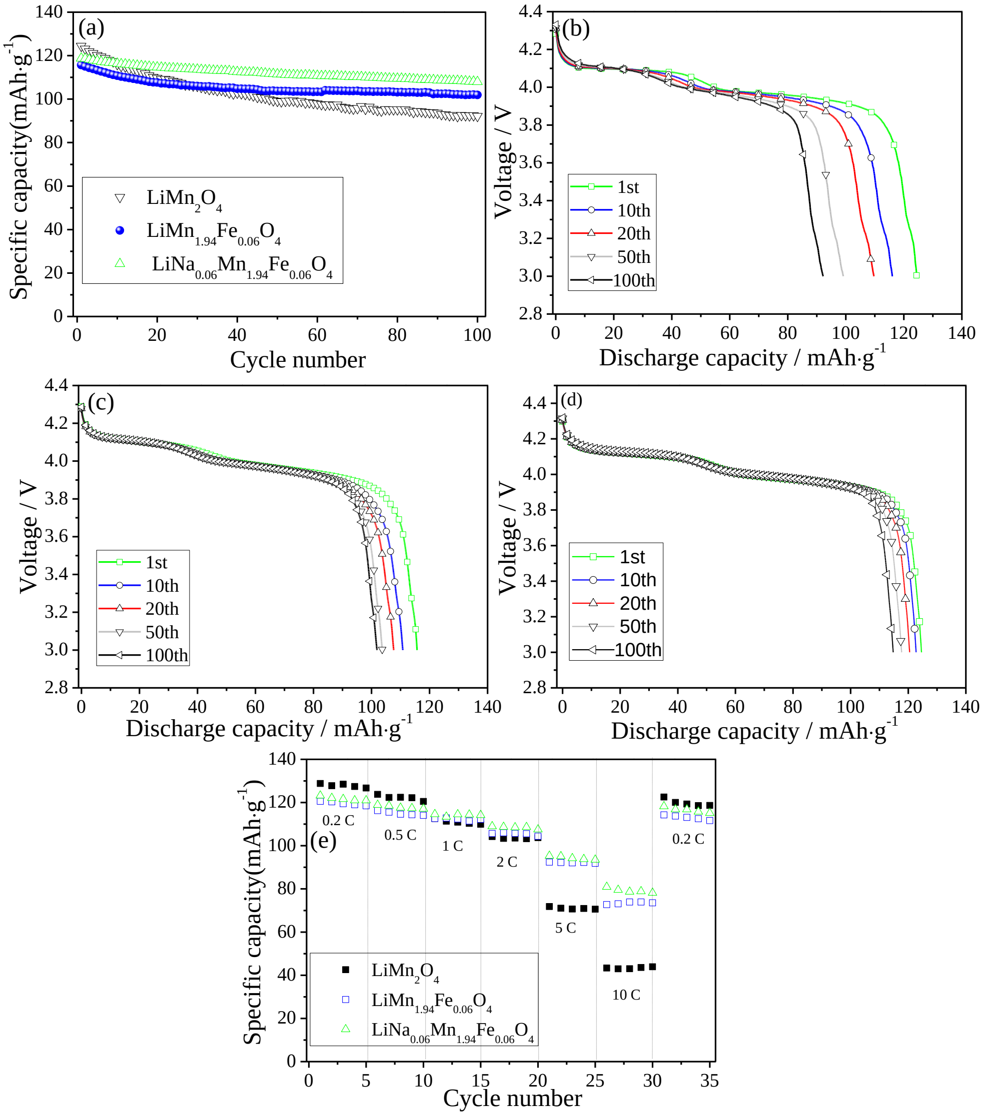

Figure 4. Cycling performances of $LiMn_2O_4$, $LiMn_{1.94}Fe_{0.06}O_4$ and $LiNa_{0.06}Mn_{1.94}Fe_{0.06}O_4$ (a); discharge capacity of $LiMn_2O_4$ (b), $LiMn_{1.94}Fe_{0.06}O_4$ (c) and $LiNa_{0.06}Mn_{1.94}Fe_{0.06}O_4$ (d) at 0.5 C rate during the different cycles; rate performances of $LiMn_2O_4$, $LiMn_{1.94}Fe_{0.06}O_4$ and $LiNa_{0.06}Mn_{1.94}Fe_{0.06}O_4$ (e).

Table 2. The discharge capacity of the samples at the 0.5 C rate in the different cycling number

Samples	Discharge capacity / *mAh·g*$^{-1}$				
	1 *st*	10 *th*	20 *th*	50 *th*	100 *th*
$LiMn_2O_4$	124.4	116.0	109.7	99.1	92.2
$LiMn_{1.94}Fe_{0.06}O_4$	115.7	110.8	107.6	103.7	101.9
$LiNa_{0.06}Mn_{1.94}Fe_{0.06}O_4$	118.8	116.4	114.7	111.5	108.0

Table 3. The discharge capacity at different current rates

Samples	Discharge capacity / *mAh·g*$^{-1}$						
	0.2 *C*	0.5 *C*	1 *C*	2 *C*	5 *C*	10 *C*	0.2 *C* (31th-35th)
$LiMn_2O_4$	128.8	120.5	109.9	103.7	70.6	43.9	118.6
$LiMn_{1.94}Fe_{0.06}O_4$	120.6	114.1	112.2	104.4	91.8	73.5	111.6
$LiNa_{0.06}Mn_{1.94}Fe_{0.06}O_4$	123.2	117.1	114.2	107.5	93.5	78.2	115.1

3.2. Electrochemistry

Cycling performances of these three samples were presented in Fig. 4(a) at 0.5 C. The initial discharge specific capacities of $LiMn_2O_4$, $LiMn_{1.94}Fe_{0.06}O_4$ and $LiNa_{0.06}Mn_{1.94}Fe_{0.06}O_4$ samples were 124.4mAh/g, 115.7mAh/g and 118.8mAh/g, respectively. After 100 cycles, corresponding specific capacities were 92.2mAh/g, 101.9mAh/g and 108.0mAh/g, and the capacity retentions were 74.12%, 88.07% and 90.91%, respectively. As seen from Table 2, with the increase of cycling, the discharge specific capacities were decreasing, while the discharge specific capacity of $LiMn_2O_4$ had the greatest reduction. During the 50th cycle, the discharge specific capacity of $LiMn_2O_4$ decreased 25.3mAh/g, that of $LiMn_{1.94}Fe_{0.06}O_4$ decreased 12.0mAh/g, while that of $LiNa_{0.06}Mn_{1.94}Fe_{0.06}O_4$ decreased only 7.3mAh/g. It indicated that the first discharge specific capacity of $LiMn_{1.94}Fe_{0.06}O_4$ would decrease despite the single doping of Fe^{3+} improved the cycling performance of the cathode materials. On the other hand, the composite doping of Fe^{3+} and Na^+ enhanced not only in the initial discharge specific capacity of the sample, but also in the cycling performance of the materials. Fig. 4(b), Fig. 4(c) and Fig. 4(d) were discharge curves of $LiMn_2O_4$, $LiMn_{1.94}Fe_{0.06}O_4$ and $LiNa_{0.06}Mn_{1.94}Fe_{0.06}O_4$ at room temperature at 0.5 C rate during the different cycles (1st, 10th, 20th, 50th, 100th). With the increase of cycles, the discharge platforms of $LiMn_2O_4$ sample gradually became shorter due to greater polarization, whereas the discharge platform of $LiNa_{0.06}Mn_{1.94}Fe_{0.06}O_4$ was the longest and steadiest [41-43], and the polarization was the smallest.

Fig. 4(e) was the rate performance charts of these three samples. Table 3 was the discharge capacity of the three samples at different current rates. As seen from the table, the discharge capacities of $LiMn_2O_4$, $LiMn_{1.94}Fe_{0.06}O_4$ and $LiNa_{0.06}Mn_{1.94}Fe_{0.06}O_4$ samples were 128.8 mAh·g^{-1}, 120.6 mAh·g^{-1} and 123.2 mAh·g^{-1} at 0.2 C rate, respectively. After each 5 times at different rates (0.2 C, 0.5 C,1 C, 2 C, 5 C, 10 C and 0.2 C), their discharge capacities reduced to 118.6 mAh·g^{-1}, 111.6 mAh·g^{-1} and 115.1 mAh·g^{-1} and the capacity retentions were 92.08%, 92.54% and 93.43%, indicating that these three materials had wonderful reversibility. $LiNa_{0.06}Mn_{1.94}Fe_{0.06}O_4$ sample had the highest capacity retention and the best reversibility. Compared with the initial discharge capacity at 0.2 C rate, the discharge capacities of $LiMn_2O_4$, $LiMn_{1.94}Fe_{0.06}O_4$ and $LiNa_{0.06}Mn_{1.94}Fe_{0.06}O_4$ at 0.5 C rate were 120.5 mAh·g^{-1}, 114.1 mAh·g^{-1} and 117.1 mAh·g^{-1}, respectively, and the capacity retentions were 93.56%, 94.61% and 95.05%, respectively. At 1C rate, the capacity retentions of the three samples were 85.33%, 93.03% and 92.69%, respectively. At 2 C rate, the capacity retentions were 80.51%, 86.57% and 87.26%, respectively. It indicated that, with the increase of rates, the discharge capacities of materials continued to reduce. The discharge capacity of $LiMn_2O_4$ reduced greatly while the $LiNa_{0.06}Mn_{1.94}Fe_{0.06}O_4$ materials still had greater capacity retention and showed excellent rate capacity. At 10 C rate, the discharge capacity of the materials $LiMn_2O_4$ was only 43.9 mAh·g^{-1}, which reduced by 84.9 mAh·g^{-1} compared with the discharge capacity in the first cycle at 0.2 C. Meanwhile, at 10 C rate, the discharge capacity of the $LiNa_{0.06}Mn_{1.94}Fe_{0.06}O_4$ cathode materials reached 78.2 mAh·g^{-1}, which was 34.3 mAh·g^{1} higher than that of $LiMn_2O_4$, so it had outstanding high-rate discharge performance. It might be partly attributed to the results that Fe^{3+} replaced Mn^{3+} partly, and the further increasing concentration of Mn^{4+}. The radius of Mn^{4+} was shorter than that of Mn^{3+}, so it could make the length of Mn-O shorter, and the bond energy of Mn-O could be increased. Therefore, it might be efficiently restrained from the structure destruction caused by the John-Teller distortion effect and made the materials keep relatively steady crystal configuration. At the same time, the doping of Na^+ improved the morphology of the materials and made particles become smaller, which promoted the ability of Li^+ deintercalation and Li^+ intercalation, thus the rate discharge performance of materials improved effectively [44].

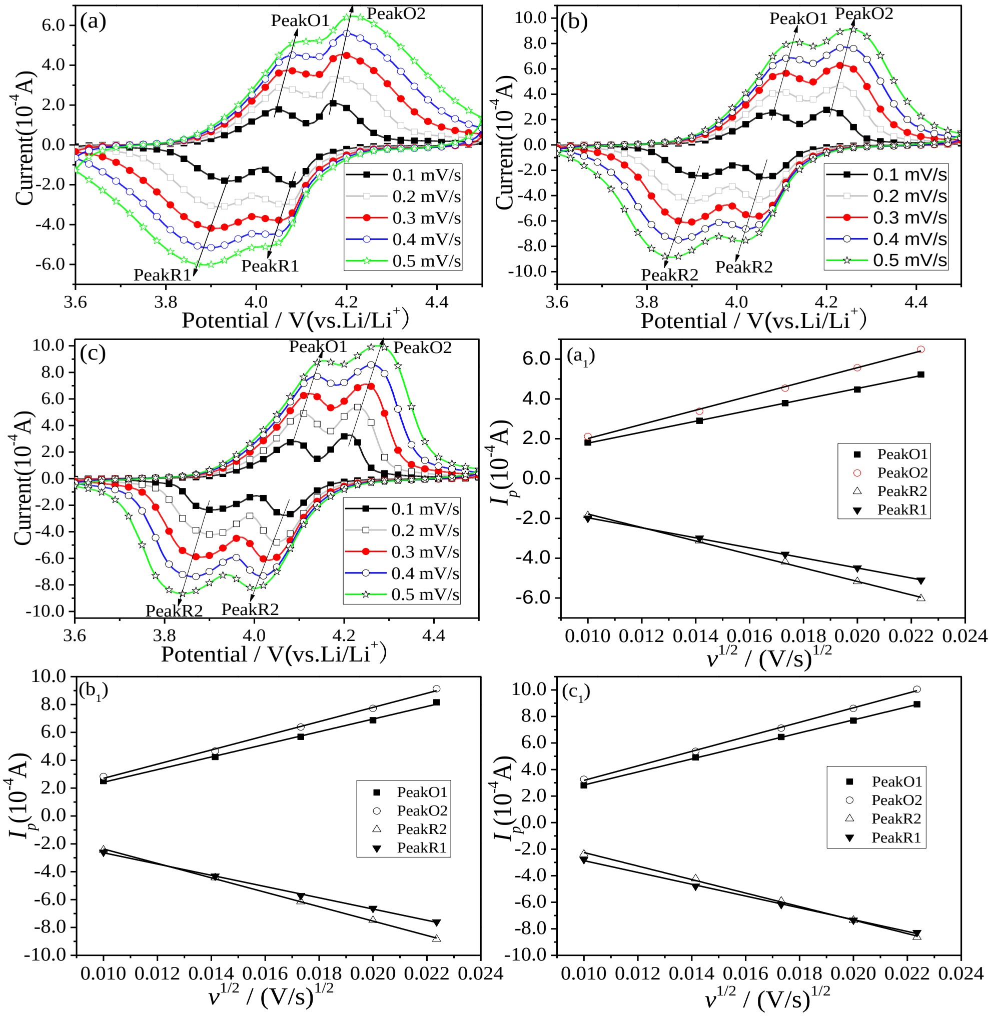

Figure 5. Cyclic Voltammetry of (a) $LiMn_2O_4$, (b) $LiMn_{1.94}Fe_{0.06}O_4$ and (c) $LiNa_{0.06}Mn_{1.94}Fe_{0.06}O_4$ at different scan rates; plots of peak current (*Ip*) vs. square root of sweep rate ($\upsilon^{1/2}$) for (a_1) $LiMn_2O_4$, (b_1) $LiMn_{1.94}Fe_{0.06}O_4$ and (c_1) $LiNa_{0.06}Mn_{1.94}Fe_{0.06}O_4$.

Table 4. The determined Li^+ diffusion coefficient for the samples

Samples	Diffusion coefficient / cm^2s^{-1}			
	PeakO1	PeakO2	PeakR2	PeakR1
$LiMn_2O_4$	5.902×10^{-12}	9.916×10^{-12}	8.975×10^{-12}	4.986×10^{-12}
$LiMn_{1.94}Fe_{0.06}O_4$	1.610×10^{-11}	2.029×10^{-11}	2.097×10^{-11}	1.278×10^{-11}
$LiNa_{0.06}Mn_{1.94}Fe_{0.06}O_4$	1.884×10^{-11}	2.343×10^{-11}	2.033×10^{-11}	1.550×10^{-11}

It can be seen from Fig. 5(a), Fig. 5(b) and Fig. 5(c) that there were 5 curves in each figure and two pairs of oxidation-reduction peaks in each curve. PeaKO1 and PeakO2 represented oxidation peaks, corresponding to the deintercalation of Li^+; PeakR1and PeakR2 represented reduction peaks, corresponding to the intercalation of Li^+. With the increase of sweeping rates, the shape of oxidation-reduction peaks changed constantly. The peak potential of PeakO1 and PeakO2 shifted toward high potential while the peak potential of PeakR1 and PeakR2 shifted toward low potential. It was because that, with the increase of scanning rates, the current density increased in the charge-discharge process and the polarization of electrode reaction increased, too. Fig. 5(a_1), Fig. 5(b_1) and Fig. 5(c_1) were plots of peak current (I_p) vs. square root of sweep rate ($\upsilon^{1/2}$).

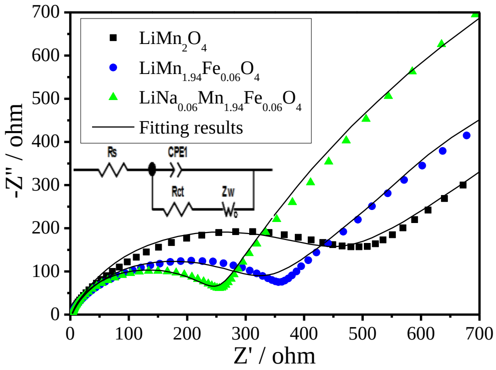

Figure 6. EIS spectra of $LiMn_2O_4$, $LiMn_{1.94}Fe_{0.06}O_4$ and $LiNa_{0.06}Mn_{1.94}Fe_{0.06}O_4$ before charge and discharge

As was seen from the figures, peak current (I_p) was linear with square root of sweep rate ($\upsilon^{1/2}$). According to the Randles-Sevcik equation [45-47], the determined Li^+ diffusion coefficient was calculated (in Table 4).

$$I_p = (2.69\times10^5)n^{2/3}AD^{1/2}v^{1/2}C_0$$

Among which I_p was peak current (A), *n* was the number of electrons transferred in the reaction (*n* = 1), *A* was the area of the electrode (cm^2) and its value was 1.766 cm^2, *D* was the diffusion coefficient of Li^+ (cm^2/s), and υ was sweep rate (V/s). C_o represented the initial concentration of Li^+ in the electrode (0.02378 mol/cm^3). As seen from Table 4, the diffusion coefficients of Li^+ of the three materials on oxidation peaks were bigger than those on reduction peaks respectively, indicating the Li^+ deintercalation process was easier than the Li^+ intercalation process. Therefore, the charging capacity of the materials was stronger than the discharging capacity. The Li^+ diffusion coefficients of $LiNa_{0.06}Mn_{1.94}Fe_{0.06}O_4$ and $LiMn_{1.94}Fe_{0.06}O_4$ on oxidation peaks and reduction peaks were twice more than that of $LiMn_2O_4$ respectively, indicating that the single doping of Fe^{3+} and the composite doping of Na^+ and Fe^{3+} made the unit cell volume larger, widened the migration channel of Li^+ as to make it easier for the deintercalation of Li^+, so the charge-discharge performance improved.

Table 5. Parameters of the equivalent circuit

Samples	R_s / $\Omega\cdot cm^{-2}$	R_{ct} / $\Omega\cdot cm^{-2}$
$LiMn_2O_4$	3.38	424.4
$LiMn_{1.94}Fe_{0.06}O_4$	3.04	316.5
$LiNa_{0.06}Mn_{1.94}Fe_{0.06}O_4$	2.79	236.9

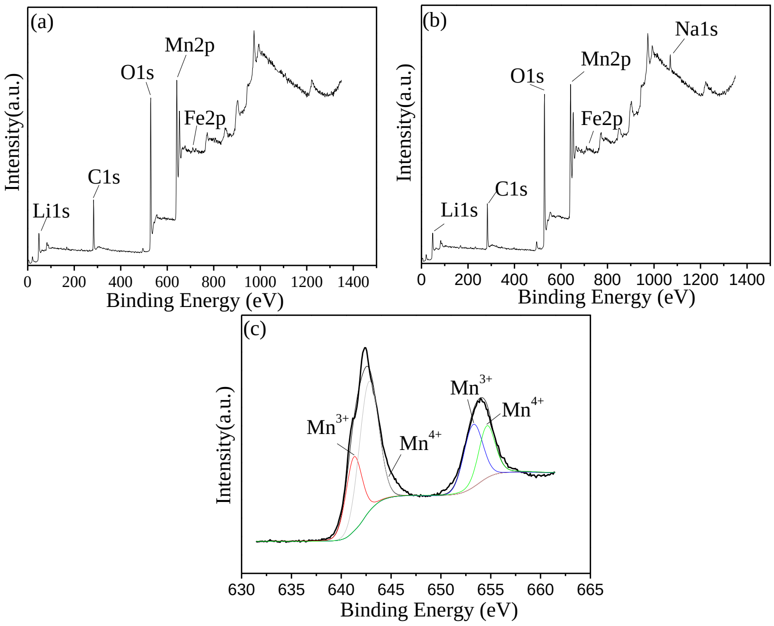

Figure 7. XPS of (a) $LiMn_{1.94}Fe_{0.06}O_4$, (b) $LiNa_{0.06}Mn_{1.94}Fe_{0.06}O_4$ and (c) Mn2p

Table 6. Specific surface area of the samples

Samples	BET surface area / $m^2\cdot g^{-1}$
$LiMn_2O_4$	2.50
$LiMn_{1.94}Fe_{0.06}O_4$	2.81

$LiNa_{0.06}Mn_{1.94}Fe_{0.06}O_4$	2.85

Fig. 6 was EIS spectra and equivalent circuit diagrams of $LiMn_2O_4$, $LiMn_{1.94}Fe_{0.06}O_4$ and $LiNa_{0.06}Mn_{1.94}Fe_{0.06}O_4$ before charge and discharge. The curves in the AC impedance were made up of three parts: (1) the ohm resistance (R_s) of high-frequency region represented the resistance for Li^+ to migrate in electrolyte; (2) semi-circles in middle and high frequency area; (3) straight lines in low frequency area. In the electrode materials, Li^+ diffusion was made up of two parts, one part flowed through surface layer and formed into equivalent capacitance (CPE_1); the other part transmitted through the surface of the electrode materials and formed into charge-transform resistance (R_{ct}), and then diffused in spinel crystal lattice and aroused Warburg resistance Z_w [48-50]. After fitting, all of the relevant figures were listed in Table 5. As seen from Table 5, compared with $LiMn_2O_4$, the ohm resistance (3.04 $\Omega\cdot cm^{-2}$) and charge-transform resistance (316.5 $\Omega\cdot cm^{-2}$) of $LiMn_{1.94}Fe_{0.06}O_4$ were relatively small. The R_s and R_{ct} of $LiNa_{0.06}Mn_{1.94}Fe_{0.06}O_4$ were only 2.79 $\Omega\cdot cm^{-2}$ and 236.9 $\Omega\cdot cm^{-2}$ respectively, which were much smaller than the other two materials. It indicated that the dual-doping Na^+ and Fe^{3+} could make the Li^+ transmit faster and diffuse more easily, resulting in better electro-chemical performance. Comparing the specific modified data reported in the literature, it can be stated that the dual-doping of Na^+ and Fe^{3+} enhanced the electrochemical property more than the single Na^+ or Fe^{3+}doped samples [51-53].

To further analyze the composition of the $LiNa_{0.06}Mn_{1.94}Fe_{0.06}O_4$ and $LiMn_{1.94}Fe_{0.06}O_4$ samples, we had made XPS and BET tests. As was seen from Fig. 7(a) and Fig. 7(b), the $LiMn_{1.94}Fe_{0.06}O_4$ sample consisted mainly of Li, Mn, Fe and O elements. While there was Na in the $LiNa_{0.06}Mn_{1.94}Fe_{0.06}O_4$ sample. In theory, the average valence state of Mn in $LiMn_2O_4$ was 3.5, through the XPS-peak-differenating analysis in Fig. 7(c), the peak area of Mn^{4+} is bigger than that of Mn^{3+}. Therefore, the content of Mn^{3+} decreased and one part of Mn in $LiMn_2O_4$ had been successfully replaced by Fe. Table 6 showed that the specific surface area of $LiNa_{0.06}Mn_{1.94}Fe_{0.06}O_4$ was largest among the three samples, thus meaning that the particle size of the $LiNa_{0.06}Mn_{1.94}Fe_{0.06}O_4$ sample was relatively small.

4. CONCLUSIONS

$LiMn_2O_4$, $LiFe_{0.06}Mn_{1.94}O_4$ and $LiNa_{0.06}Mn_{1.94}Fe_{0.06}O_4$ were prepared by spiny spherical MnO_2 precursor synthesized by hydrothermal method. The research revealed that the composite doping of Na^+ and Fe^{3+} could effectively reduce the charge transfer resistance and improve the Li^+ diffusion coefficient, thus it could evidently enhance the rate performance and cycling stability of the materials. Therefore, the composite doping with Na^+ and Fe^{3+} was an effective way to improve the electrochemical performance of $LiMn_2O_4$ cathode materials. It is will be an attractive application for practical high-power Li-ion battery

ACKNOWLEDGEMENTS
This work was financially supported by the National Science Foundation of China (Grant No. 51364008) and the Science, Technology Research Projects of Guangxi institution of higher education

(Grant No. 2013ZD030) and the Guangxi Natural Science Foundation (Grant No. 2014GXNSFAA118046).

References

1. X. Li, B. Zhou, W. Wang, Z. Xu, N. Li , *J. Alloys Compd*., 706(2017) 109.
2. L. Xing, W. Li, C. Wang, F. Gu, M. Xu, *J. Phys. Chem*., B 113(2009) 16602.
3. S.H. Yoo, C.K. Kim, *Ind. Eng. Chem. Res.*, 48(2009) 9941.
4. K. Mizushima, P.C. Jones, P.J. Wiseman, *Mater. Res. Bull*., 15(1980) 789.
5. X. Yang, L. Shen, B. Wu, Z. Zuo, D. Mu, *J. Alloys Compd*., 639(2015) 464.
6. K. Sekai, H. Azuma, A. Omaru, S. Fujita, H. Imoto, *J. Power Sources*., 43(1993) 244.
7. M.S. Park, H.H. Sang, C.N. Sang, *J. Electroceram*., 17(2006) 655.
8. M. Balandeh, S. Asgari, *J. Nanomater*., 2010(2010) 143.
9. Q. Zhu, S. Zheng, X. Lu, *J. Alloys Compd*., 654(2016) 391
10. P. Kalyani, N. Kalaiselvi, *Sci. Technol. Adv. Mater*., 6(2005) 703.
11. A.K. Padhi, K.S. Nanjundaswamy, J.B. Goodenough, *J. Electrochem. Soc*., 144(1997) 1194.
12. W.S. Yoon, J. Hanson, J. Mcbreen, XQ. Yang, *Electrochem. Commun*., 8(2006) 862.
13. T. Aoshima, K. Okahara, C. Kiyohara, K. Shizuka, *J. Power Sources*., 97(2001) 380.
14. J. Jang, K. Du, Y. Cao, *J. Alloys Compd*., 577(2013) 142.
15. T.F. Yi, C.L. Hao, C.B.Yue, RS. Zhu, J. Shu, *Synthetic Metals.*, 159(2009) 1260.
16. J.W. Lee, J.I. Kim, S.H. Min, *J. Power Sources*., 196(2011) 1493.
17. X. He, J. Li, Y. Cai, Y. Wang, J. Ying, *J. Power Sources*., 150(2005) 222.
18. S. Suzuki, M. Tomita, S. Okada, H. Arai, *J. Phys. Chem. Solids*., 57(1996) 1856.
19. R. Thirunakaran, A. Sivashanmugam, S. Gopukumar, *Mater. Res. Bull*., 43(2008) 2129.
20. L. Xiao, Y. Zhao, Y. Yang, Y. Cao, X. Ai, *Electrochim. Acta*,.54(2008) 550.
21. T.F. Yi, Y. Xie, M.F. Ye, L.J Jiang, R.S Zhu , *Ionics*,. 17(2011) 389.
22. T.F. Yi, J. Mei, Y.R. Zhu, *J. Power Sources*., 316(2016) 105.
23. L. Xiong, Y. Xu, W. Wu, P. Lei, T. Tao, *Electron. Mater. Lett*., 10(2014) 790.
24. H.J. Bang, V.S. Donepudi, J. Prakash, *Electrochim. Acta*., 48(2002) 451.
25. T. Tsuji, M. Nagao, Y. Yamamura, *Solid State Ionics*., 154(2002) 386.
26. A.M.A. Hashem, *Preparation. Ionics*., 10(2004) 212.
27. A. Hashem, A. Abdel-Latif, H. Abuzeid, HM. Abbas, H. Ehrenberg, *J. Alloys Compd*., 509(2011) 9674.
28. S.H. Lim, J. Cho, S.H. Lim, *Electrochem. Commun*.,10(2008) 1481.
29. X. Wang, Y. Li, *J. Am. Chem. Soc.*, 124(2002) 2881.
30. M. Kitta, T. Akita, M. Kohyama, *AIP Adv*., 6(2016) 359.
31. Y.L. Ding, J. Xie, G.S. Cao, T.J. Zhu, H.M .Yu , *Adv. Funct. Mater*., 21(2011) 355.
32. X.M. He, J.J. Li, Y. Cai, Y. wang, J. Ying, *J. Solid State Electrochem*., 9(2005) 444.
33. E. Hosono, T. Kudo, I. Honma, H. Matsuda, H. Zhou, *Nano lett*., 9(2009)1051.
34. S. Lim, J. Cho, *Chem. Commun*. 37(2008) 4474.
35. J. Luo, Y. Wang, H. Xiong, Y. Xia, *Chem. Mater.*, 19(2007) 4795.
36. K.M. Shaju, P.G. Bruce, *Chem. Mater*., 20(2008)5562.
37. D. Tonti, M.J. Torralvo, E. Enciso, I. Sobrados, J. Sanz, *Chem. Mater*., 20(2008) 4790.
38. W. Yang, G. Zhang, J. Xie, L. Yang, Q. Liu, *J. Power Sources*., 81(1999) 415.
39. A. Yuan, L. Tian, W. Xu, Y. Wang, *J. Power Sources*., 195(2010) 5038.
40. Q. Liu, K. Du, H. Guo, *Electrochim. Acta.*, 90(2013) 357.
41. S. Kuwabata, S. Masui, H. Yoneyama, *Electrochim. Acta*., 44(1999) 4600.
42. M.R. Palacin, Y. Chabre, L. Dupont, M. Hervieu, P. Strobel, *J. Electrochem. Soc*., 147(2000) 853.
43. N. Ozawa, K. Donoue, T. Yao, *Electrochem. Solid-State Lett*., 6(2003) A108.
44. M.E. Spahr, P. Novak, B. Schnyder, O. Haas, R. Nesper, *J. Electrochem. Soc*., 145(1998) 1113.

45. J.R. Dahn, J. Jiang, L.M. Moshurchak, M.D Fleischauer , C.Buhrmester , *J. Electrohem. Soc*., 152(2005) A1283.
46. H. Liu, L.J. Fu, H.P. Zhang, J. Gao, C.Li , *Electrochem. Solid-State Lett*., 9(2006) A529.
47. T. Nakamura, K. Sakumoto, M. Okamoto, S. Seki , Y. Kobayashi, *J. Power Sources*., 174(2007) 435.
48. S. Chen, C. Mi, L. Su, B.Gao , Q.Fu , *J. Appl. Electrochem*., 39(2009) 1943.
49. L. Feng, Y. Chang, L. Wu, T. Lu , *J. Power Sources*., 63(1996) 149.
50. Q.C. Zhuang, T. Wei, L.L. Du, Y.L. Cui , L. Fang , *J. Phys. Chem*. ,C 114(2010) 8614.
51. F. Sun, Y. Xu, *J. Alloys Compd*., 584 (2014) 538.
52. Q. Wang, X. Zhang, Y. Xu, D. Liu, H. Dong and Y. Zhang, *RSC. Adv*., 5(2015)75333.
53. Y. Lee, So-Hyun. Park, John B. Parise, and Clare. P. Grey, *Chem. Mater*., 14(2012)194.